High-Crystallinity BiOCl Nanosheets As Efficient Photocatalysts for Norfloxacin Antibiotics Degradation

Mingxia Li *, Bo Wang *, Zhenzi Li *

Posted Date: 16 May 2023

doi: 10.20944/preprints202305.1099.v1

Keywords: photocatalysis; BiOCl; nanosheets; high-crystallinity

Article

High-Crystallinity BiOCl Nanosheets as Efficient Photocatalysts for Norfloxacin Antibiotics Degradation

Dongxue Song [1], Mingxia Li [1,*], Lijun Liao [2], Liping Guo [2], Haixia Liu [2], Bo Wang [2,*] and Zhenzi Li [2,*]

[1] School of Chemistry and Materials Science, Key Laboratory of Functional Inorganic Material Chemistry, Ministry of Education of the People's Republic of China, Heilongjiang University, Harbin 150080, P. R. China

[2] Shandong Provincial Key Laboratory of Molecular Engineering, School of Chemistry and Chemical Engineering, Qilu University of Technology (Shandong Academy of Sciences), Jinan, Shandong, 250353, P. R. China

* Correspondence: limingxia@hlju.edu.cn (M.L.); wangb123@qlu.edu.cn (B.W.); zzli@qlu.edu.cn (Z.L.)

Abstract: The stability of semiconductor catalysts is a very important property in the field of catalytic reactions. Materials necessitate resistance to mechanical abrasion and chemical erosion for better overall performance. In this work, high crystallinity BiOCl nanosheets were prepared by a simple hydrothermal method. The photocatalysts demonstrate full UV light absorption ability and excellent photocatalytic norfloxacin degradation performance. 84 % of highly toxic norfloxacin were photocatalytically eliminated within 180 min. The internal structure and surface chemical state of BiOCl were analyzed by SEM, TEM, Raman, FTIR, UV-vis, XPS, and other techniques. Such high crystallinity makes BiOCl molecules closely arranged and the molecular chains strongly connected, thus exhibiting a high level of photocatalytic stability and recyclability.

Keywords: photocatalysis; BiOCl; nanosheets; high-crystallinity

1. Introduction

With the rapid development of industry on a global scale, environmental pollution is becoming increasingly serious. Global environmental pollution and ecological damage have caused many toxic and harmful pollutants in water sources and soils [1–7]. The environmental self-cleaning rate is relatively slow and incomplete, resulting in the long-term existence of harmful substances in the environment. In recent years, photocatalytic technology, as an energy-saving and efficient green technology, has shown advantages for pollutant degradation compared to traditional wastewater purification methods in the treatment of industrial, pharmaceutical, and dyestuff wastewater [8–13]. Therefore, the development of inexpensive photocatalysts for wastewater purification in real conditions is very important for the sustainable development of human society.

Bismuth chloride oxide (BiOCl) is gradually coming into our view as an important ternary photocatalyst with a layered structure of alternating $[Bi_2O_2]^{2+}$ layers and double Cl^- atomic layers along the *c*-axis [14–16]. The layered structure can hinder electron-hole recombination due to the weaker van der Waals force interactions between the $[Bi_2O_2]^{2+}$ layer and the double Cl^- atomic layer [17–19]. This structure can also produce uneven charge distribution between the cation and anion layers, the polarization of the constituent atoms and orbitals, internal electric field, and the surface capture of photogenerated carriers [20–24]. The atomic and orbital polarized intra-layer structure has enough polarized orbital space, which directly promotes the electron-hole separation rate and enhances the activity of the photocatalyst [25]. Liao et al. [26] synthesized BiOCl nanowires using a simple and safe method to change the conventional two-dimensional structure of BiOCl into a one-dimensional structure with a high spreading ratio and exposure of a large number of surface active sites. This structure leads to the curing of the wide bandgap of BiOCl, thereby creating a narrow

 doi:10.20944/preprints202305.1099.v1

bandgap semiconductor with a bandgap position of about 1.92 eV. The photocatalysts present enhanced visible light absorption ability and rhodamine B dye degradation activity with up to 80 % removal efficiency in 90 min. Also, Zhang et al. [27] assembled three-dimensional nanoflowers with nanosheets of highly exposed (001) facets. Its UV absorption spectrum exhibited an absorption edge out at 358 nm, from which the estimated bandgap gap was 3.46 eV. The photocatalytic removal efficiency of rhodamine B by BiOCl nanoflowers was up to 98 % within 60 min, which was 34 % higher than that of BiOCl nanoflakes. BiOCl photocatalysts exhibit valuable photocatalytic activity in the UV range due to the wide bandgap. However, its photocatalytic characteristics are rarely represented individually in various studies.

Herein, high crystallinity BiOCl was synthesized using the conventional hydrothermal method with $Bi(NO_3)_3{\cdot}5H_2O$ as the Bi source to form a large number of 1 ~ 2 μm nanosheets. The high crystallinity suggests that most of the molecular chains are tightly ordered and compact in the microscopic state, thus leading to enhanced intermolecular forces. In macroscopic phenomena, it shows high catalyst stability. The chemical surface states and molecular internal motion trajectories of BiOCl based on its high crystallinity were thoroughly studied.

2. Experimental section

2.1. Chemicals

Bismuth nitrate pentahydrate ($Bi(NO_3)_3{\cdot}5H_2O$) was purchased from Shanghai Dibai Biotechnology Co., Ltd, Potassium chloride (KCl) was obtained from Tianjin Guangfu Technology Development Co., Ltd, All the above chemicals are analytical grade and used without further purification.

2.2. Synthesis

6 mmol $Bi(NO_3)_3{\cdot}5H_2O$ and 6 mmol KCl were first added to 32 mL distilled water. Then the solution was stirred for 30 min. The above solution was subsequently transferred to a 50 mL PTFE-lined stainless steel autoclave for continuous reaction at 160 ℃ for 12 h (24 h). The collected sample was denoted as BiOCl (BiOCl 24 h).

2.3. Photocatalytic performance test

The photocatalytic activity of BiOCl was tested in the norfloxacin ($C_{16}H_{18}FN_3O_3$) degradation process. A 300 W Xe lamp (Beijing Porphyry Co., Ltd.) with an AM 1.5 filter was used as the light source. The calibrated light intensity was 100 MW cm^{-2} before the measurements. Typically, the prepared photocatalyst (50 mg) was first added to 50 mL of norfloxacin solution (10 mg/L). To achieve adsorption-desorption equilibrium, the suspension was placed in the dark at room temperature for 5 min. Then, the suspension was irradiated and vigorously stirred. 4 mL of the reaction mixture was taken every 5 min and filtered through a 0.22 μm microporous filter to remove the photocatalyst from the solution. The UV-Vis absorption spectra of the residual norfloxacin were recorded with a UV-Vis spectrophotometer (Shanghai Mepro Delta UV-1800 BPC).

3. Results and Discussion

3.1. Morphology and microstructure

The synthesis process of creating highly crystalline BiOCl nanosheets using a one-step hydrothermal method is described in Figure 1. As described in Figure 1, $Bi(NO_3)_3{\cdot}5H_2O$ is used as the Bi source, while the Cl^- is provided by KCl. The BiOCl nanosheet structure can be obtained by continuous heating at 160 ℃ in a pure water solvent for 12 h.

Preprints (www.preprints.org) | NOT PEER-REVIEWED | Posted: 16 May 2023 doi:10.20944/preprints202305.1099.v1

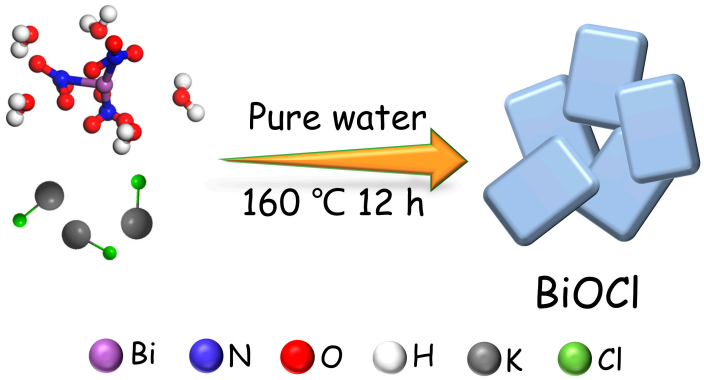

Figure 1. Scheme for the formation of BiOCl.

Figure 2a and b show scanning electron microscopy (SEM) images of BiOCl, showing that the BiOCl structure is a two-dimensional (2D) nanosheet with uniform morphology. The width of the nanosheet ranges from 1 to 2 μm. The formed nanosheets are clustered together by electrostatic interactions [28–31]. In the magnified image, it can be observed more clearly that the surface of the material is smooth and free from particles, thus increasing the wear resistance of the material. The SEM image of BiOCl 24 h was shown in Figure 2c. Although it has a similar nanosheet structure, its morphology is irregular and has tiny impurities.

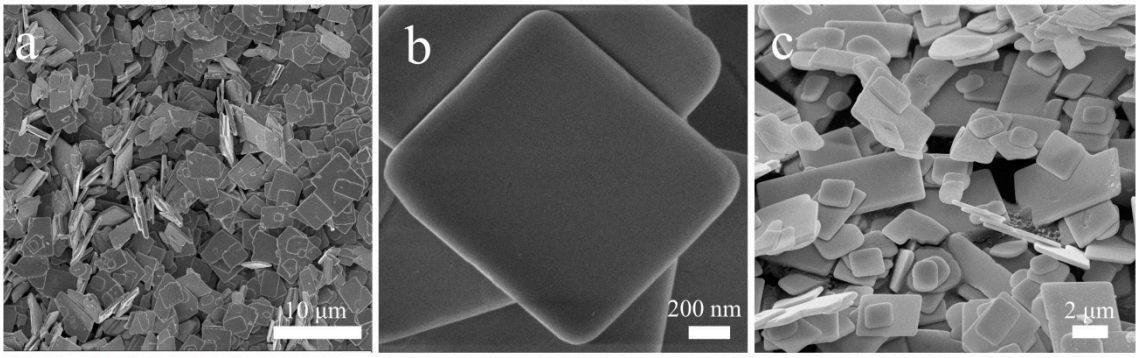

Figure 2. SEM images of BiOCl (a, b) and BiOCl 24 h (c).

The transmission electron microscopy (TEM) images of Figure 3a,b present the nanosheet structure of single-phase BiOCl and the appearance of regular and clear arrays of square diffraction spots in selected areas of electron diffraction (SAED) images of the corresponding nanosheets (Figure 3c), indicating that BiOCl is a single-crystal material [32]. The high-resolution transmission electron microscopy (HRTEM) in Figure 3d demonstrates clear lattice stripes. The exposed (102) crystal plane of BiOCl has a lattice spacing of 0.268 nm.

Preprints (www.preprints.org) | NOT PEER-REVIEWED | Posted: 16 May 2023 doi:10.20944/preprints202305.1099.v1

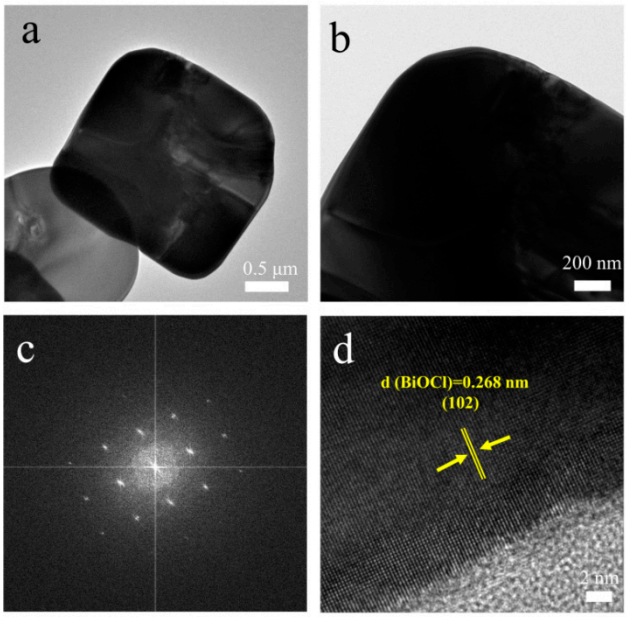

Figure 3. TEM (a, b), SAED (c) and HRTEM (d) images of BiOCl.

The crystal structures of BiOCl and BiOCl 24 h were analyzed by the XRD pattern in Figure 4a. All the diffraction peaks correspond well to the BiOCl tetragonal structure crystalline phase, which has very high crystallinity and no other spurious peaks, indicating that there is only one substance of BiOCl in the material. Its corresponding standard card is JCPDS no. 82-0485 and the space group is P4/mmm (NO. 129). The cell parameters of BiOCl are a= b = 3.878 Å and c = 7.403 Å. The highly crystalline BiOCl and BiOCl 24 h have eleven major diffraction peaks in the XRD patterns, 2 θ = 12.0, 24.2, 25.9, 32.5, 33.5, 36.6, 41.0, 46.7, 49.8, 55.2 and 58.7° , and the diffraction peaks are located on the crystal plane of (001) (002) (101) (110) (102) (003) (112) (200) (113) (104) (212), respectively. High crystallinity also indicates excellent dimensional stability and tight molecular alignment within the structure that is less prone to fracture. To further investigate the surface state of the samples, Raman tests were performed on the BiOCl catalysts to determine the stretching or vibrational modes of the molecules. Three main diffraction peaks appear in the Raman (Raman) spectrum of Figure 4b, among which 144 and 199 cm^{-1} bands belong to the Bi-X bond stretching vibrations within A_{1g} and E_g of BiOCl, respectively. The peak at 395 cm^{-1} can be ascribed to the E_g and B_{1g} energy bands generated by the motion of O atoms [33,34]. To get a clear understanding of the structural atomic bonding within BiOCl, Fourier transform infrared spectroscopy (FTIR) was utilized to detect the chemical bonds in BiOCl molecules. As shown in Figure 4c, the vibrational peak at 1621 cm^{-1} can be attributed to the stretching and bending motion of the hydroxyl (–OH) group, which is caused by the surface hydration phenomenon. The strong characteristic peak at 526 cm^{-1} is generated by the stretching of the Bi-O bond within BiOCl [35]. The formation of highly crystalline BiOCl was further verified. The optical properties were measured by ultraviolet-visible diffuse reflectance (UV-vis), as shown in Figure 4d, using UV-visible diffuse reflectance spectroscopy. BiOCl has a continuous absorption band in the range of 360-800 nm. It can be determined that the maximum absorption wave edge occurs at about 378 nm. Thus the bandgap position can be obtained by Equation 1:

$$E_g\ (eV) = 1240/\lambda \quad (1)$$

The estimated bandgap value of BiOCl is about 3.37 eV (Figure 4e), which is suitable for light absorption in the UV region. Although UV light accounts for a relatively small fraction of solar energy, such a forbidden bandwidth can absorb UV light sufficiently to achieve the catalytic application of BiOCl in the UV region. As shown in Figure 4f, the nitrogen adsorption-desorption isotherm was obtained for the analysis of the porous structure. In the relative high-pressure region, BiOCl exhibits type IV isotherm and H hysteresis loop. Type IV isotherm is similar to type II isotherm in the relative low-pressure region, but is prone to capillary coalescence in the region of higher

Preprints (www.preprints.org) | NOT PEER-REVIEWED | Posted: 16 May 2023 doi:10.20944/preprints202305.1099.v1

relative pressure, making the latter half of the curve climb sharply [36]. It also indicates that BiOCl nanosheets are mesoporous structures. The specific surface area, pore volume, and pore diameter of BiOCl catalysts are further derived from the Brunauer-Emmett-Teller (BET) theory to give a total surface area of 1.0 m^2g^{-1}. The pore volume and pore diameter of BiOCl is 0.002 cm^3g^{-1} and 16.6 nm, respectively.

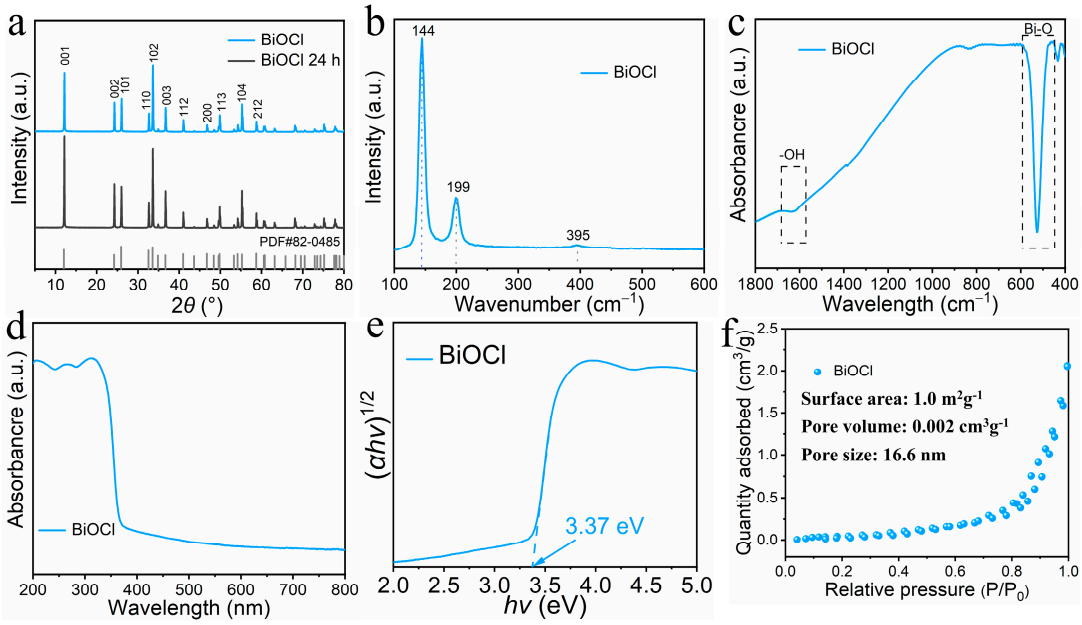

Figure 4. XRD pattern (a) of BiOCl and BiOCl 24 h. Raman spectra (b), FT-IR (c), UV-vis diffuse absorption spectra (d), bandgap (e), and N_2 adsorption-desorption isotherm of BiOCl.

In addition to the internal structural analysis of BiOCl, we further investigated the surface elements of BiOCl and its chemical state. The X-ray photoelectron spectra (XPS) in Figure 5 perfectly demonstrate the elemental states in BiOCl. Among them, the fitted peaks of Bi^{3+} fall in the binding energy of 164.45 and 159.15 eV (Figure 5a), and the two peaks belong to Bi $4f_{7/2}$ and Bi $4f_{5/2}$ orbitals, respectively [37]. The fitted peaks of O elements are at 532.28 and 529.88 eV binding energy (Figure 5b), which can be ascribed to oxygen-containing components adsorbed to the surface of BiOCl and the hydroxyl and lattice oxygen in BiOCl. [38]. The two fitted peaks for elemental Cl at 201.95 and 200.31 eV (Figure 5c) correspond to the Cl $2p_{3/2}$ and Cl $2p_{1/2}$ orbitals, respectively, confirming the presence of Cl^- [39]. The elemental composition was also analyzed in the XPS full spectrum (Figure 5d), containing characteristic peaks of the orbitals of three elements, Bi, O, and Cl. Bi 4p, O 1s, Bi 4d, C 1s, Cl 2p, Bi 4f, and Bi 5d orbitals can be observed in the full spectrum. Among them, C 1s is from the carbon in air adsorbed on the surface of the sample at the time of testing. For Bi elements, Bi 4f has the highest intensity, the smallest peak width, and the best symmetry, and is the mainline spectrum of Bi elements. There are also weak line spectra of Bi 4p, Bi 4d, and Bi 5d. Since Bi elements have multiple internal electrons, multiple XPS signals of Bi elements were produced. In addition, there is no interference from any other elements in BiOCl. It indicates that the sample synthesized by BiOCl is clean and free of impurities. The XPS valence band spectra of BiOCl also provided the valence band structure information of BiOCl. The energy corresponding to the valence band position is around 2.21 eV obtained in Figure 5e. As shown in Figure 5f, the Mott-Schottky curves tested at three frequencies of 1.0, 1.5, and 2.0 kHz to determine the flat-band valence. The intercept of the curve in the *x*-axis can be derived from the flat-band potential is -0.99 V. It can be seen that BiOCl's is a positive slope curve, which proves that this material is an n-type semiconductor, and the participation in the conductivity is dominated by free electrons. The carrier concentration can be obtained from Equation 2:

Preprints (www.preprints.org) | NOT PEER-REVIEWED | Posted: 16 May 2023 doi:10.20944/preprints202305.1099.v1

$$N_d = \left(\frac{2}{e_0 \varepsilon \varepsilon_0}\right)\left(\frac{d\frac{1}{C^2}}{dV}\right)^{-1} \quad (2)$$

Where e_0 is the charge per unit charge, ε is the relative permittivity, ε_0 is the vacuum permittivity, C is the interfacial capacitance, and V is potential. We obtain the vacuum dielectric constant of BiOCl ε_0 = 55 [40]. The carrier concentration of BiOCl is calculated as $N_d = 1.22\times10^{19}$. Furthermore, the flat-band potential can be deduced from the position of the conduction band (CB) by using Equation 3:

$$E\ (\mathrm{RHE}) = E\ (\mathrm{Ag/AgCl}) + 0.0591\mathrm{pH} + 0.197 \quad (3)$$

The calculated CB value of BiOCl falls at -0.38 V. As a classical photocatalyst suitable for degradation, the oxidation capacity of BiOCl itself deserves to be studied in depth.

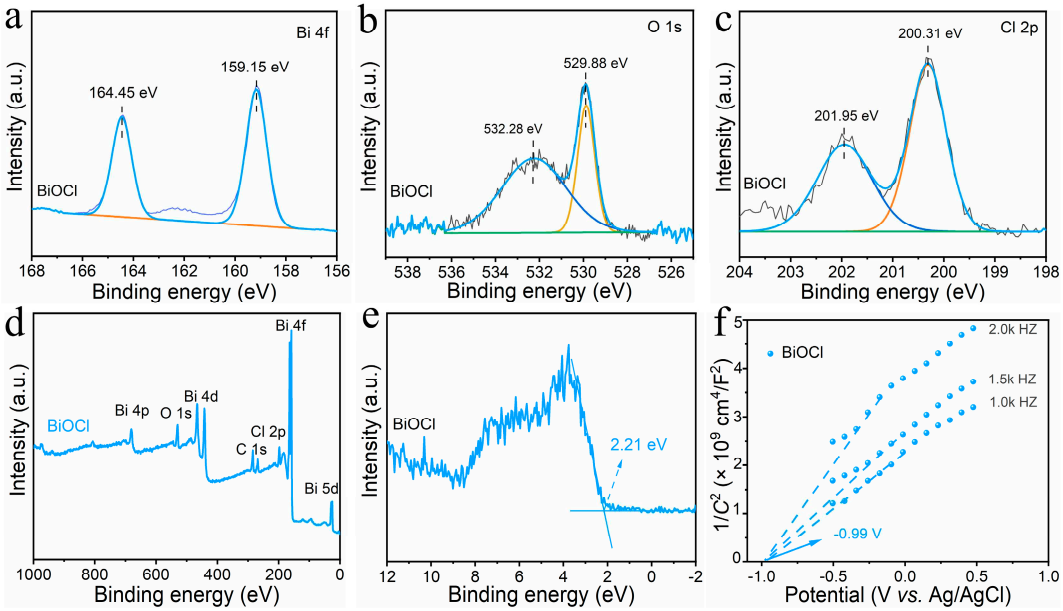

Figure 5. XPS spectra of Bi 4f (a), O 1s (b), Cl 2p (c). Full-scale XPS spectra (d) valence band spectra (e) and Mott–Schottky plot (f) of BiOCl.

3.2. Photocatalytic activity and mechanism

Although the content of antibiotics in water resources is not high, it is still harmful to human beings and cannot be ignored. In this work, the degradation of norfloxacin in an aqueous solution was carried out under simulated sunlight irradiation using BiOCl as the photocatalyst. As can be seen in Figure 6a, after one hour of dark treatment to reach an adsorption balance of norfloxacin on BiOCl, the degradation rate of norfloxacin reached 84 % within 180 min under light irradiation, while the degradation rate of norfloxacin over BiOCl 24 h was only 72 %, indicating that BiOCl under 12 h reaction conditions possessed a better degradation ability. And the rate constants of 0.010 min^{-1} and 0.007 min^{-1} for BiOCl and BiOCl 24 h were obtained from the rate curves, respectively (Figure 6b). The rate constant of BiOCl was about 1.43 times higher than that of BiOCl 24 h, which once again highlighted that the BiOCl degradation process was efficient. To examine the recyclability of the BiOCl material, five cycling experiments were performed (Figure 6c). After five consecutive degradations, the catalytic activity remained almost unchanged. Such stability of BiOCl material indicates that it can be recycled after several times of wastewater treatment. In the radical capture experiments in Figure 6d, Tert-butanol (*t*-BuOH) was used to capture hydroxyl groups, potassium iodide (KI) to capture holes, silver nitrate ($AgNO_3$) to capture electrons, and benzoquinone (BQ) to capture superoxide anions, respectively [41,42]. Compared with the blank experiment, we know that the main active substances in the BiOCl system are electrons and superoxide anions. In conclusion,

Preprints (www.preprints.org) | NOT PEER-REVIEWED | Posted: 16 May 2023 doi:10.20944/preprints202305.1099.v1

BiOCl photocatalysts have both great photocatalytic activity and excellent recyclability, which further confirms the feasibility of BiOCl materials in practical applications.

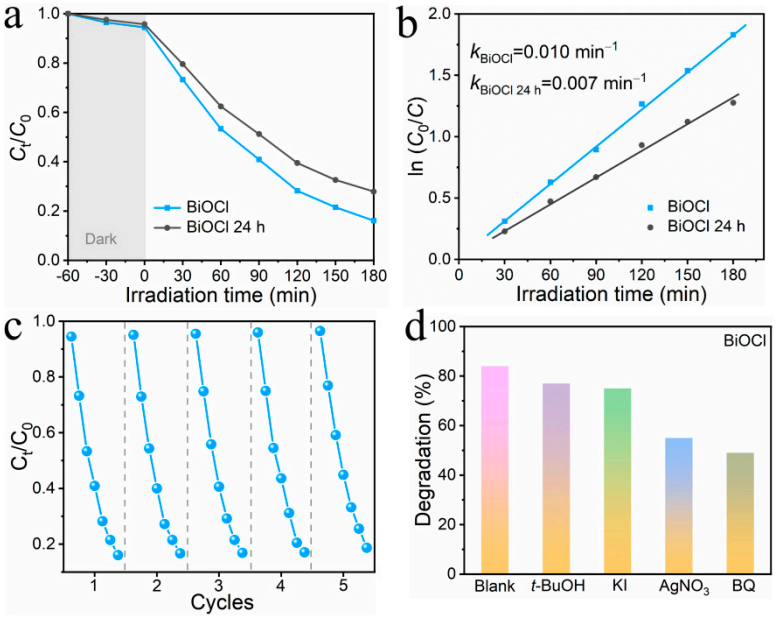

Figure 6. Photocatalytic degradation curves of norfloxacin (a), rate curves (b) of BiOCl and BiOCl 24 h. Cyclic photodegradation curve for norfloxacin (c) of BiOCl. Inhibition of norfloxacin degradation by free radical scavengers in the BiOCl system.

As shown in the photocatalyst mechanism in Figure 7, the separation of electrons and holes occurs in highly crystalline BiOCl nanosheets under light irradiation. The excited electrons are transferred from the valence band to the conduction band, and the holes are left in the valence band. The CB value of BiOCl obtained from equation 3 is -0.38 V and the bandgap value obtained from equation 1 is 3.37 eV. Therefore, the VB position can be obtained to be 2.99 V. The hydroxide (OH^-) at the VB position loses an electron and is converted into a hydroxyl radical ($^{\bullet}OH$), while the oxygen (O_2) molecule at the CB position accepts an electron and produces the reduction product superoxide anion ($^{\bullet}O_2^-$). Both of them play an important role in the photocatalytic reaction. Norfloxacin was photocatalytically converted to carbon dioxide, water, and other small molecule impurities over BiOCl materials. The photocatalytic carrier complex is prevented under the conditions of photoexcitation, which promotes the oxidation ability of BiOCl, increases the active site, captures the norfloxacin molecule, and then degrades it into a non-toxic and harmless substance. Such BiOCl with high crystallinity not only has excellent photocatalytic activity but also presents great wear and chemical resistance [43].

Preprints (www.preprints.org) | NOT PEER-REVIEWED | Posted: 16 May 2023 doi:10.20944/preprints202305.1099.v1

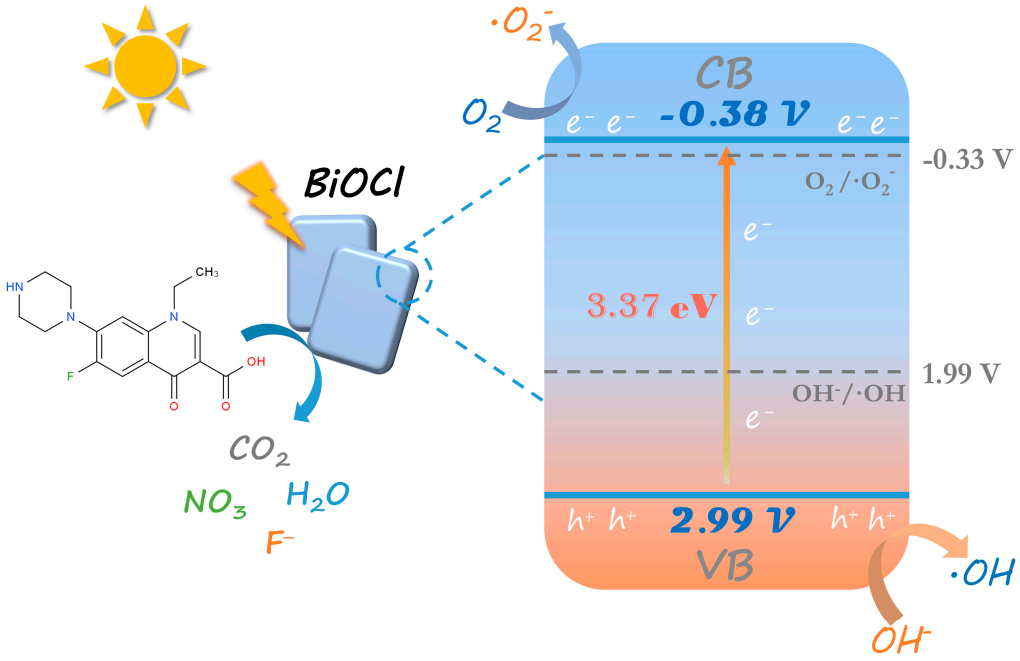

Figure 7. Photocatalytic mechanism of high crystallinity BiOCl under sunlight irradiation.

4. Conclusions

In summary, we synthesized highly crystalline BiOCl nanosheets by a simple hydrothermal method. The BiOCl photocatalysts exhibited better degradation performance compared with the materials obtained via other identical preparation methods. Under solar irradiation, BiOCl degraded 10 mg/L norfloxacin in 180 min. The degradation rate is 1.17 times higher than that of BiOCl 24 h, with a rate constant 1.43 times higher than that of BiOCl 24 h. Such good catalytic activity can be summarized for the following reasons: (1) The wider bandgap absorbs UV light from sunlight and excites the electron-hole pairs in the semiconductor structure to produce photogenerated carriers, one uses the photogenerated holes to convert OH^- to $^{\bullet}OH$ in water to further oxidize the adsorbed pollutants. The other combines electrons with O_2 to form $^{\bullet}O_2^-$, thereby exerting an oxidizing effect. The two kinds of photogenerated carriers work together to stimulate the oxidation ability of BiOCl, achieving excellent degradation efficiency. (2) The high crystallinity structure of BiOCl possesses strong molecular chains to achieve a molecular dense stacking effect, which makes the BiOCl structure strong and stable, and resistant to wear and tear and chemical reagent contamination, and good cycling stability for degrading pollutants. Such well-performing BiOCl photocatalysts provide the basis and ideas for the development of subsequent complexes.

Declaration of Competing Interest: The authors declare that they have no known competing financial interests or personal relationships that could have appeared to influence the work reported in this paper.

Acknowledgements: We gratefully acknowledge the support of the National Natural Science Foundation of China (22205124, 22275103), the Heilongjiang Province Natural Science Foundation (LH2021B021), and the Development Plan of Youth Innovation Team in Colleges and Universities of Shandong Province.

References

1. R. I. Kaiser, L. Zhao, W. Lu, et al., Nat. Commun. 13 (2022) 786.
2. J. Ran, H. Zhang, S. Fu, et al., Nat. Commun. 13 (2022) 4600.
3. J. Theerthagiri, S. J. Lee, K. Karuppasamy, et al., J. Hazard. Mater. 412 (2021) 125245.
4. J. D. Xiao, R. Li, H. L. Jiang, Small Methods 7 (2023) 2201258.
5. J. Ye, C. Wang, C. Gao, et al., Nat. Commun. 13 (2022) 6612.
6. H. Yi, D. Huang, L. Qin, et al., Appl. Catal. B: Environ. 239 (2018) 408-424.
7. J. Zhou, J. Li, L. Kan, et al., Nat. Commun. 13 (2022) 4681.

8. S. Fang, X. Lyu, T. Tong, et al., Nat. Commun. 14 (2023) 1203.
9. H. Li, C. Cheng, Z. Yang, et al., Nat. Commun. 13 (2022) 6466.
10. T. Liu, Z. Pan, K. Kato, et al., Nat. Commun. 13 (2022) 7783.
11. Y. Liu, C. H. Liu, T. Debnath, et al., Nat. Commun. 14 (2023) 541.
12. A. Tavasoli, A. Gouda, T. Zahringer, et al., Nat. Commun. 14 (2023) 1435.
13. Q. Zhang, S. Gao, Y. Guo, et al., Nat. Commun. 14 (2023) 1147.
14. B. Qin, M. Z. Saeed, Q. Li, et al., Nat. Commun. 14 (2023) 304.
15. Q. D. Gibson, T. D. Manning, M. Zanella, et al., J. Am. Chem. Soc. 142 (2020) 847-856.
16. G. Hao, C. Zhang, Z. Chen, et al., Adv. Funct. Mater. 32 (2022).
17. D. Li, Y. Sun, M. Li, et al., ACS Nano 16 (2022) 16966-16975.
18. X. Wu, N. Liu, M. Wang, et al., ACS Nano 13 (2019) 13109-13115.
19. L. Wang, X. Zhao, D. Lv, et al., Adv. Mater. 32 (2020) e2004311.
20. S. Huang, G. Zhang, F. Fan, et al., Nat. Commun. 10 (2019) 2447.
21. Y. Shi, J. Li, C. Mao, et al., Nat. Commun. 12 (2021) 5923.
22. Y. Sun, Y. Wang, E. Wang, et al., Nat. Commun. 13 (2022) 3898.
23. H. Gu, G. Shi, L. Zhong, et al., J. Am. Chem. Soc. 144 (2022) 21502-21511.
24. Y. Wang, J. An, L. Qi, et al., J. Am. Chem. Soc. 145 (2023) 864-872.
25. S. Guo, X. Li, J. Li, et al., Nat. Commun. 12 (2021) 1343.
26. X. Liao, X. Lan, N. Ni, et al., ACS Appl. Nano Mater. 4 (2021) 3887-3892.
27. X. Zhang, L. Yuan, F. Liang, et al., Environ. Chem. Lett. 18 (2019) 243-249.
28. F. Nakagawa, M. Saruyama, R. Takahata, et al., J. Am. Chem. Soc. 144 (2022) 5871-5877.
29. Y. Zhu, P. Shao, L. Hu, et al., J. Am. Chem. Soc. 143 (2021) 7897-7902.
30. E. E. Greciano, J. Calbo, E. Orti, et al., Angew. Chem. Int. Ed. Engl. 59 (2020) 17517-17524.
31. H. Wan, Q. Xu, J. Wu, et al., Angew. Chem. Int. Ed. Engl. 61 (2022) 202208577.
32. S. Weng, B. Chen, L. Xie, et al., J. Mater. Chem. A 1 (2013) 3068.
33. G. Liu, B. Wang, X. Zhu, et al., Small 18 (2022) 2105228.
34. L. Wang, R. Wang, T. Qiu, et al., Nano Lett. 21 (2021) 10260-10266.
35. X. Cao, A. Huang, C. Liang, et al., J. Am. Chem. Soc. 144 (2022) 3386-3397.
36. T. Hiratsuka, H. Tanaka, M. T. Miyahara, ACS Nano 11 (2017) 269-276.
37. W. Wang, M. Favaro, E. Chen, et al., J. Am. Chem. Soc. 144 (2022) 17173-17185.
38. P. Chen, P. Zhang, X. Kang, et al., J. Am. Chem. Soc. 144 (2022) 14769-14777.
39. R. Jiang, G. Lu, M. Wang, et al., Appl. Catal. B: Environ. 299 (2021).
40. Y. Nalawade, J. Pepper, A. Harvey, et al., ACS Appl. Electron. Mater. 2 (2020) 3233-3241.
41. Q. Liu, H. Li, H. Zhang, et al., Chin. Chem. Lett. 33 (2022) 4756-4760.
42. X. Nie, G. Li, S. Li, et al., Appl. Catal. B: Environ. 300 (2022).
43. Q. Li, J. Ren, Y.-j. Hao, et al., Appl. Catal. B: Environ. 317 (2022).